

A framework for studying turbulent boundary layer interaction with anisotropic compliant surface

By A. Shahriar[†] AND K. Shoele[†]

A computational framework is proposed for studying the interaction of turbulent boundary layer with a compliant anisotropic coating inspired by dolphin skin. Dolphin skin is a natural anisotropic surface with longitudinal rows of stiff dermal ridges and controllable dermal papillae. The papillae can be regulated by blood supply and innervation. Here, we are interested in determining whether the anisotropic design of dolphin skin can regulate the coherent structures of the turbulent boundary layer. Given that the dynamics of the turbulent boundary layer over flexible surface are affected by several parameters, a hierarchical modeling approach is introduced. A resolvent flow analysis is formulated for the most critical conditions. In addition, a coupled fluid-structure interaction model has been developed for dolphin-inspired complex anisotropic viscoelastic solid layers and tested for sample flow conditions.

1. Introduction

In pursuit of an optimal compliant surface, researchers have studied dolphin skin and tried to design artificial layers that closely mimic its behavior (Kramer 1962; Fisher & Blick 1966, e.g.). Most of the researches on this topic are motivated by Kramer (1962) where it was suggested that a specific bio-inspired compliant surface design can substantially reduce drag in the boundary layer flow. Subsequent theoretical and experimental studies have been conducted to understand better the role of compliant surface/layer in laminar boundary layer flow transition. However, the effects of a flexible surface on a fully developed turbulent boundary layer (TBL) are still not well understood and remain controversial (e.g. Xu *et al.* 2003), and there have been conflicting results from theoretical, numerical, and experimental studies (e.g. Ivanov *et al.* 2017).

Dolphin skin is a natural prototype for a wide range of flexible coatings. It is made up of three compliant layers: an epidermis (top layer), a spanwise periodic dermis (middle layer), and a spanwise periodic hypodermis (bottom layer) (see Figure 1). The epidermis layer is composed of highly viscoelastic materials. The dermis contains blood vessels, nerves, and connective tissue. The fibrous nature of dermal papillae is responsible for generating micro-scale anisotropic behavior, while the spanwise placement of the dermis and hypodermis layers results in macro-scale anisotropy. These features induce damping and anisotropic effects and modify the propagation of deformation waves. Moreover, the dermal papillae structure allows the skin to perform active and semi-active flow control tasks. With increased swimming speed, the dermal structure can potentially modify the formation of longitudinal vortices in the TBL. The longitudinal features of dolphin skin are similar to those of shark and swordfish skins. However, compared to shark skin, dolphin skin is more complicated; this is correlated with the broader range of swimming

[†] Department of Mechanical Engineering, FAMU-FSU College of Engineering, Tallahassee

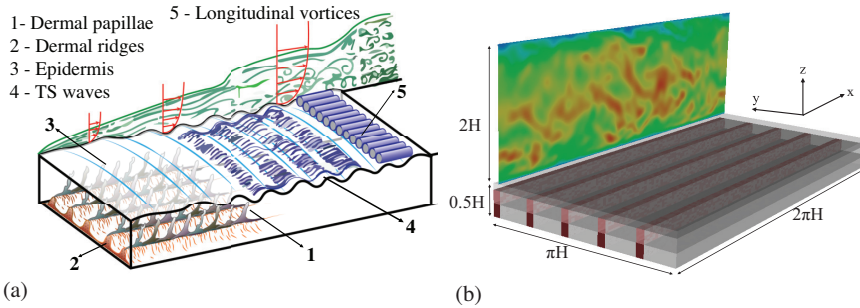


FIGURE 1. (a) 3D schematic of dolphin skin and boundary layer over the compliant skin [adopted from Babenko (2021)]; and (b) computational model of dolphin skin.

speeds in dolphins compared to sharks and the need to adjust to diverse flow conditions (Fish & Rohr 1999).

Investigating the interaction between the turbulent flow and a compliant surface is a complex process. Rather than avoiding the interaction, the dynamics of the solid can be exploited to influence the boundary layer. Previous studies have been conducted to understand and elucidate the underlying relationship between turbulent flow properties and a compliant layer's motion. Benschop *et al.* (2019) identifies critical parameters that govern the interaction of the turbulent flow over the compliance surface. Other theoretical models have also been proposed to simplify the interaction (Duncan 1986). More recently, Esteghamatian *et al.* (2022) studied the coupled fluid-structure interaction (FSI) response of a compliant coating and noted that sheets of vorticity are lifted by the inflectional velocity at the troughs when there is a certain relation between the phase speed of elastic surface waves and the advection speed of the near-wall fluctuations. Nevertheless, there is no theoretical description of the system that adequately captures the interaction between the flow and wave propagation in multi-material and multi-layers compliant coatings. This study explores new aspects of this problem and develops a multilevel computational framework to study aspects of the turbulent boundary layer interaction with an anisotropic compliant coating inspired by the dolphin skin.

2. Formulation and computational setup

All the variables are non-dimensionalized using one-half the channel height H and the wall-friction velocity $u_\tau = \sqrt{\tau_w/\rho_f}$ as characteristic length and velocity, where τ_w is the wall shear stress averaged over time on the top horizontal plane. The Reynolds number is defined as $Re_\tau = u_\tau H/\nu$. This results in the following non-dimensional equations describing the conservation of mass and momentum as,

$$\nabla \cdot \mathbf{u} = 0, \quad \frac{\partial \mathbf{u}}{\partial t} + \nabla \cdot (\mathbf{u} \otimes \mathbf{u}) = \nabla \cdot \boldsymbol{\sigma}, \quad (2.1)$$

where $\boldsymbol{\sigma} = -p\mathbf{I} + (1/Re_\tau) [\nabla \mathbf{u} + \nabla^T \mathbf{u}]$ is the stress tensor. The solid region is governed by

$$\frac{\partial^2 \mathbf{d}}{\partial t^2} = \frac{M^*}{C_a} \nabla \cdot \boldsymbol{\sigma} + \mathbf{f}_s, \quad \text{with } C_a = \frac{\rho_f u_\tau^2}{E} \text{ and } M^* = \frac{\rho_f}{\rho_s}, \quad (2.2)$$

where C_a is the Cauchy number and M^* is the mass number. Here, \mathbf{f}_s is the external force density acting on the solid. In the present study, to account for geometric non-

linearity and large deformation, the Green–Lagrangian strain tensor \mathbf{E} and second Piola Kirchhoff stress tensor \mathbf{S} are used, defined as

$$\mathbf{S} = J\mathbf{F}^{-1}\boldsymbol{\sigma}\mathbf{F}^{-T} \text{ and } \mathbf{E} = \frac{1}{2}(\mathbf{F}^T\mathbf{F} - \mathbf{I}), \quad (2.3)$$

where \mathbf{F} is the deformation gradient between the initial position and the current position, and J is the determinant of \mathbf{F} . Depending on the material, a particular constitutive relation is used to calculate \mathbf{S} based on \mathbf{E} and $\partial\mathbf{E}/\partial t$. At the interface of the flow and structure, the kinematic and dynamic conditions are used (Paidoussis 1998).

2.1. Dolphin-skin structure and the problem setup

To study the role of compliant surface anisotropy on momentum exchange at the solid–fluid interface, we use a model geometrically and structurally similar to dolphin skin. The model is made of three horizontal layers: (a) the upper layer representing epidermis of dolphin skin; (b) the middle layer mimicking the structure of dermal papillae; and (c) the lower layer similar to dermal ridges in dolphin skin, reflecting the description provided in Babenko (2021). The problem setup is schematically shown in Figure 1b. Here, we select the thickness of the upper layer to be one-half that of the other layers, following the work of Carpenter *et al.* (2000). The dermal papillae and dermal ridge layers are spanwise-periodic with Δs constant spacing. Based on the biological prototype, it is assumed that the dermal papillae layer is made up of cylindrical hair-type structures placed on top of ridges at a certain angle. The angle of dermal papillae changes depending on the location of measurement along the body of a dolphin, and since each has nerve endings and lymphatic and blood capillaries, it is argued that their kinetic behavior can be controlled to tune the skin dynamic responses in different flow conditions. The bio-inspired model here closely follows the dolphin-skin characteristics, so we can explore whether this specific structural design can act as a wave-guide with a particular frequency band gap that attenuates disturbances with a certain amplitude and frequency, similar to newly proposed phononic materials (Patil & Matlack 2021).

While computational models are good candidates for studying the FSI of particular cases, they are prohibitively expensive to explore the role of system parameters (such as material properties and ridge spacing). To reduce the complexity of the problem, one can use linearized equations and employ reduced-order modeling approaches such as resolvent analysis (Luhan *et al.* 2015). In the original resolvent analysis over a flat surface, the effect of disturbances was modeled as an additive source of stochastic excitation in the NS equations to reach an input–output model. The original resolvent analysis explores important wavenumber–frequency combinations using the singular value decomposition of the forcing–response transfer function named as the resolvent operator. The high-gain resolvent modes are often nicely correlated with the dynamically important flow features such as the near-wall cycle. This formulation is further modified for the system with spatially periodic features like riblets (Luhan & Chavarin 2019; Ran *et al.* 2021). In this work, we explore resolvent analysis as a reduced-order model for analyzing and designing soft and hard anisotropic coating systems.

2.2. Unified approach for soft and hard anisotropic compliant coatings

Based on the anisotropic characteristics of the compliant surface and the magnitude of the hydrostatic pressure, three solid response regimes are expected: (1) small static deflection and high-frequency oscillation around the flat interface (hard coating), (2) large static deflection due to hydrostatic pressure but small dynamic oscillation around

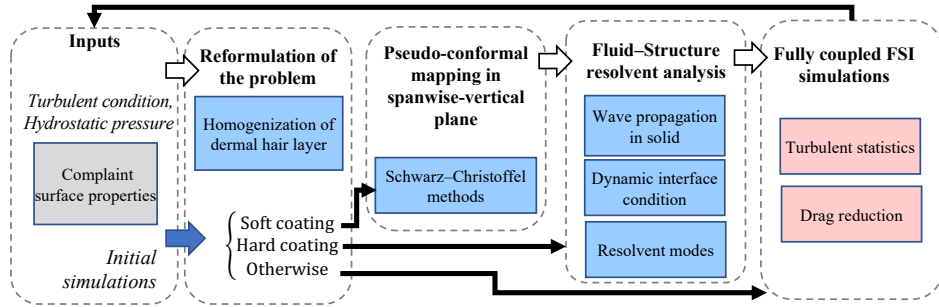


FIGURE 2. An analysis framework for studying TBL interaction with a compliant surface.

the statically deformed interface (soft coating), and (3) the situation in which both static deflection and dynamic deflection are large and comparable. Resolvent analysis is used here as a reduced-order model of the first two response regimes. The third scenario, on the other hand, requires a fully coupled FSI mode; this case will be explained in later sections. The framework is summarized in Figure 2.

3. Linear model

3.1. Homogenization approach for anisotropic compliant layers

Elastic isotropic material models are used for ridges and skin materials. However, a homogenized transversely isotropic model is adopted to represent the papillae layer. It is assumed papillae have similar orientation over the ridges and are placed close to each other with separation distance l' , which is much smaller than the thickness of the hair layer in the spanwise direction ($l' \ll w_p$). This allows us to employ the homogenization approach and variational principles to characterize the effective elastic moduli of the composite layer (Francfort & Murat 1986). In this approach, we solve for a rank 3 tensor $\chi^{kl} = \chi_i^{kl}$ in a unit periodic cell using the finite element method (Tong & Mei 1992) and employ this tensor to define the macro homogenized elastic modulus in the rotated coordinate of hairs as

$$\mathcal{C}'_{ijkl} = \langle \mathbb{C}'_{pqmn} (\delta_{pi}\delta_{qj} + \epsilon_{pq}(\chi^{ij})) (\delta_{mk}\delta_{nl} + \epsilon_{mn}(\chi^{kl})) \rangle, \quad (3.1)$$

where $\langle \cdot \rangle$ represents the averaging operator over a unit cell, ϵ is the elastic strain and \mathbb{C}'_{pqmn} is the elastisty of each material. Finally, we employ coordinate transformation between the attached coordinate of the papilla and the global Cartesian coordinate by the orthogonal tensor (\mathbf{Q}) to reach final elastic modulus (\mathcal{C}).

3.2. Conformal mapping

For the soft coatings, prior solid simulations with the imposed hydrostatic pressure are performed to identify the shape of the interface. Then, the problem is reformulated in a transformed domain, where the interface is a flat horizontal interface between the flow and solid domains. Mapping between the two domains uses the generalized Schwarz-Christoffel transformation (SCT) (Floryan & Zemach 1993). SCT is a special conformal mapping technique suitable for the current work, which does not change the kinetic energy of the flow during the mapping (Wang & Shoele 2021). In this approach, the mapping between the physical domain $\hat{z} = y + iz$ and the transformed domain $\hat{\zeta} = \xi + i\eta$

is achieved via the generalized SCT for periodic domains as

$$\frac{d\hat{z}}{d\hat{\zeta}} = e^{i\theta(\Delta s)} \exp \left[- \int_{u=-\Delta s/2}^{\Delta s/2} \log \sin \frac{\pi}{\Delta s} (\hat{\zeta} - u) d\theta(u) \right], \quad (3.2)$$

where u represents the distance on the interface in the transformed domain ($-\Delta s/2 \leq u \leq \Delta s/2$). With analytical conformal mapping, we can relate the gradient of any scalar in the transformed domain to its gradient in the physical domain. In the rest of this report, to simplify the discussion, we consider only the resolvent model for the hard compliant layer: with the above formulation, the same procedure can be followed for soft compliant layers.

3.3. Wave propagation and resolvent operator

A linear spectral wave propagation model is employed to model the composite compliant layer. A three-layer anisotropic medium is assumed wherein the material properties of the first layer are homogeneous while the other two layers contain spanwise periodic material properties. We introduce a smoothed Heaviside step function $H(y)$ to define the material distribution in the spanwise direction, $\mathcal{C} = H\mathcal{C}_1 + (1-H)\mathcal{C}_2$, where subscript 1 identifies the base material and subscript 2 identifies the stiffer material. The spanwise-periodic H function can be equivalently approximated as $H(y) = \sum_{m \in \mathbb{Z}} a_m \exp(im\omega_y y)$, where ω_y is the fundamental spatial frequency of the ridges ($\omega_y = 2\pi/\Delta s$). Each layer is further divided into N_i sublayers, each with a thickness h , a spanwise-periodic density ρ , and anisotropic (yet symmetric) constitutive matrix $\mathcal{D} = d_{ij}$ ($i, j = 1 \dots 6$). A contracted (Voigt) notation is assumed to simplify the derivation. Within each layer, the equation of motion is

$$\rho \ddot{\mathbf{U}} - \mathbf{L}^T \mathcal{D} \mathbf{L} \mathbf{U} = \mathbf{0}, \quad (3.3)$$

where $\mathbf{U}_s^T = [U_x, U_y, U_z]^T$ is the displacement vector and \mathbf{L} is related to the gradient operator (Kausel 1986). The displacement field in each thin sublayer is approximated by a linear expression of displacement vectors at the interfaces of sublayers, $\tilde{\mathbf{U}} = [\mathbf{U}_1^T, \dots, \mathbf{U}_N^T]^T$.

A harmonic solution is assumed for $\tilde{\mathbf{U}}$ in the form of

$$\tilde{\mathbf{U}}(x, y, t) = \sum_{n \in \mathbb{Z}} \hat{\mathbf{U}}_n(k_x, k_y, \omega) e^{-i(\omega t - k_x x - k_n y)} \quad \text{with} \quad \begin{cases} k_x \in \mathbb{R}, \\ k_n = n \kappa_s + k_y, \\ k_y \in (-\kappa_s/2, \kappa_s/2), \end{cases} \quad (3.4)$$

where we assumed normal modes in x and Bloch waves in the spanwise direction determined from the product of $e^{ik_y y}$ and a $\kappa_s = 2\pi/\Delta s$ periodic function (Chavarin & Luhar 2020). After lengthy derivation (skipped here for brevity), the harmonics of the interface traction and displacement can be related analytically and symbolically written as,

$$[\hat{d}_x, \hat{d}_y, \hat{d}_z]_{-n \dots n}^T = \hat{\mathcal{H}}(k_x, k_y, \omega) [\hat{\tau}_{xz}, \hat{\tau}_{yz}, -\hat{p}]_{-n \dots n}^T \quad \text{on } \partial\Omega_{FS}, \quad (3.5)$$

where $[\]_n^T$ implies the n th Bloch harmonic at the interface. This expression is used to derive the modified resolvent analysis based on Chavarin & Luhar (2020) and Luhar *et al.* (2015) for the wavenumber-frequency combinations of interest, $\mathbf{k} = (\omega, k_x, k_y + n\kappa_s)$ for $n = -n_{max} \dots n_{max}$. After eliminating the pressure, we can write $\hat{\mathbf{u}}_\kappa = \mathbf{H}_\kappa \hat{f}_\kappa$. Here, $\hat{\mathbf{u}}_\kappa = [\hat{\mathbf{u}}_{-n_{max}} \dots \hat{\mathbf{u}}_{n_{max}}]^T$ and notation κ implies the coupled system of Fourier modes associated with the individual wavenumber-frequency combination. The resolvent operator can be simplified using proper weighting functions,

$$\mathbf{H}_\kappa^W = \sum_n \boldsymbol{\psi}_{\kappa,n} \boldsymbol{\sigma}_{\kappa,n} \boldsymbol{\phi}_{\kappa,n}^H, \quad (3.6)$$

where $\mathbf{f}_{\kappa,n} = \mathbf{W}_f^{-1} \boldsymbol{\phi}_{\kappa,n}$ and $\mathbf{u}_{\kappa,n} = \mathbf{W}_u^{-1} \boldsymbol{\psi}_{\kappa,n}$ are force and response modes for sorted singular values of $\boldsymbol{\sigma}_{\kappa,n}$ (Luhar *et al.* 2015). Previous studies show that the extreme rank-1 approximation is still able to capture key structural and statistical features of smooth-walled turbulent flows; therefore, we anticipate that the rank-1 approximation will be a good indicator of the dynamics of our system as well.

While the proper exploration of all the problem parameters requires substantially more effort, here we present initial results for two primary vortical coherent structures: the energetic near-wall (NW) cycle and the spanwise rollers resembling Kelvin-Helmholtz vortices. These flow structures are selected because of previous research on ripples, although other flow structures might need further research. The first important coherent vortical structure was the near wall cycle which based on the smooth boundary layer flow has the wavenumber-frequency triple of $[k_x, k_y, \omega/k_x] = [2\pi Re_\tau/10^3, 2\pi Re_\tau/10^2, 10]$ (Robinson 1991). This mode is associated with the structures near $y^+ = 15$ and has been the subject of previous studies (Chavarin & Luhar 2020). The second coherent structure investigated is associated with different ω and k_x but with a zero spanwise wavenumber $k_y = 0$. In each case, the roles of ridge separation, skin stiffness, ridge stiffness, hair tilting angle, and hair density were tested. We found that the initial tests do not follow what has been observed for solid ripples and other choices of wavenumber-frequency could be more dynamically important. For this reason, the results from these tests are skipped here, and only certain observations are given. First, much more refined tests of the wavenumber-frequency triple are required before one can identify the most dynamic form of the interactions. Secondly, the most energetic modes share the similar features of both of the above vortical coherent structures. In the next step of this work, the framework discussed here can be used to carefully interrogate the parameters and identify the most consequential solid design and its associated response and forcing mode shapes.

4. Nonlinear model

A high-order sharp immersed boundary method based on a weighted least-square error minimization is employed for the flow solver (Seo & Mittal 2011). The flow solver is based on a sixth-order compact central finite difference with eighth-order implicit spatial filtering and a third-order total variation diminishing Runge-Kutta (RK3-TVD). The neo-Hookean model based on the strain energy density function $W = C_1(I_1 - 3 - 2 \ln J + D_1(J - 1)^2)$ is assumed to define stress according to $\mathbf{S} = \partial W / \partial \mathbf{E}$. A finite deformation viscoelasticity model is used based on Reese & Govindjee (1998). In the results shown here, we tentatively assumed that skin has a large viscosity but the dermal ridge and papillae have zero viscosity. The nonlinear solid governing equations are solved using a parallel finite element and advanced in time with the Hilber-Hughes-Taylor (HHT) time integration scheme (Hilber *et al.* 1977). The model is validated for canonical test cases.

In this report, the partitioned approach is used for investigating the turbulent flow over flexible surfaces. A body force is assumed in the fluid domain to maintain a constant bulk velocity and random fluctuations are added to the initial conditions to accelerate the flow transition to the turbulent state. All the results shown here are after the transient behavior passed. The domain dimensions shown in Figure 1b are selected according to Esteghamatian *et al.* (2022). The friction Reynolds number (Re_τ) is set to 180 and a

Layer	Type	Density, ρ_s/ρ_f	Shear modulus, $G/\rho_f U^2$		Bulk modulus, $B/\rho_f U^2$	
			Fully coupled	Soft coating	Fully coupled	Soft coating
Epidermis	Viscoelastic	1.0	0.5		25	75
Dermal papillae	Viscoelastic	1.0	1.5		25	400
Dermal ridge	Viscoelastic	1.0	7.5		25	400
					800	800

TABLE 1. Material properties for different layers of the finite element model (FEM) model. The parameters of hard coating are similar to fully coupled case.

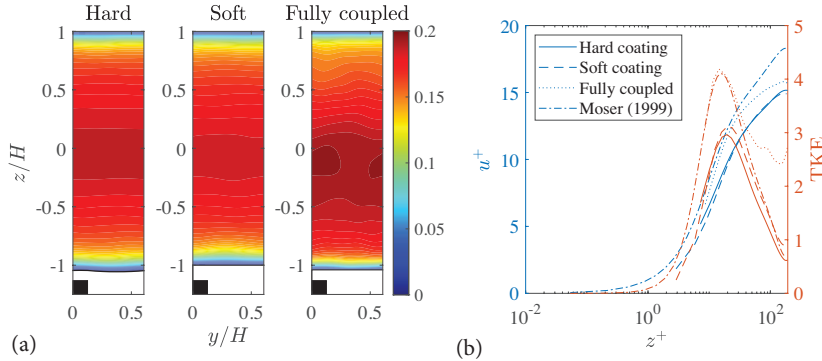


FIGURE 3. (a) Contour plot of the time-averaged streamwise velocity field between two consecutive ridges on the spanwise plane and (b) mean velocity \bar{u} and the non-dimensionalized turbulent kinetic energy (TKE) profiles of different simulation cases.

moderate fluid grid of $241 \times 83 \times 129$ is used for the flow simulation. For the solid modeling, $100 \times 20 \times 50$ elements are used. The width of the ridge is fixed as $0.125H$, and the gap between two neighbor ridges is chosen to be $0.5H$.

4.1. One-way coupled simulations

One-way coupled simulations are fast techniques allowing us to explore a wide range of parameters and identify parameters that could lead to strong interactions and interesting dynamics. Two groups of one-way coupling simulations are conducted here: (1) hard coating and (2) soft coating.

For the hard-coating simulations, the surface deformation is very small and does not change the topology of the fluid domain. Under this assumption, one can ignore the displacement of the solid–fluid interface, but must satisfy the velocity boundary condition at the interface. For this setup, the material properties used in the simulation is listed in Table 1. Here, because of higher bulk modulus and shear modulus, the timescales of the flow and solid were different and a strong momentum/energy transfer at the interface was not found. It would be challenging to find optimum parameters for this simple setup with trial and error, but the simulations if combined with the insights from the resolvent analysis can capture the optimum parameters of the hard coatings. The time-averaged streamwise velocity between two consecutive ridges is shown in Figure 3(a). The average streamwise velocity profile is compared with other test cases as well. The black zone on the bottom left shows the position of the ridge.

In the case of soft coating, at first, a volumetric average pressure is calculated inside the channel and then, this pressure is gradually applied to the top surface of the flexible

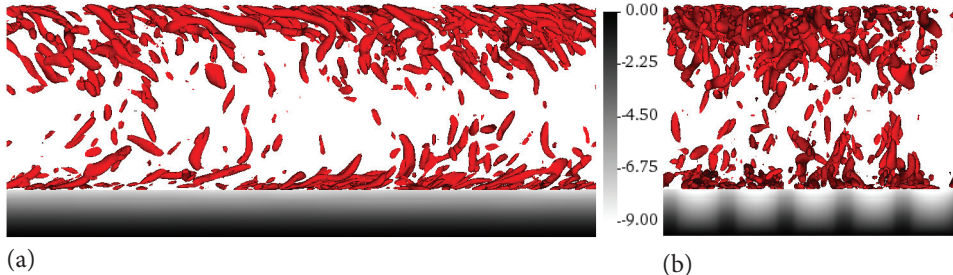


FIGURE 4. Vortical structures and displacement. Iso-surface: Q-criterion and Contour: displacement; (a) the side view on xz plane, (b) the front view on yz plane.

material. Once the skin is deformed and reached a steady state configuration, the deformed shape of the top surface is recorded. The average amount of static deformation is $d_z u_\tau / \nu = 8.91$ for a static pressure of $p/\rho u_\tau^2 = 4.6352 \times 10^3$. The ridges will help the skin to develop a wavy shape in the spanwise direction, and the measured height difference between a peak and a valley is 2.34 viscous wall units. For higher pressure, the static deflection can be modified to provide a design factor that can be leveraged for control of turbulent flow structures. In the second stage, the channel flow simulation was run using the recorded shape of the surface. The statistical data were collected during the simulation, and the time-averaged velocity is shown in Figure 3. The effect of surface curvature as small as 2.34 wall units can be seen in the averaged streamwise velocity component.

4.2. Fully coupled FSI simulation

We used an iterative coupling approach, wherein the data (e.g, force, displacement, and velocity) are exchanged between the solvers. The parameters used for the test case shown here are given in Table 1. Figure 4 shows the Q-criterion of the flow field. The turbulent vortical structures can be easily recognized at the top and bottom boundaries. The top boundary is rigid, and qualitatively more turbulent coherent structures are identified on this side compared to the bottom boundary layer, which is interacting with a compliant surface. The gray-scale contour shows the displacement of the thick flexible dolphin skin. The surface deformation has been further investigated by looking at the time history of deflection on two perpendicular lines in the streamwise and spanwise directions. The streamwise line is at the middle of the domain, exactly on top of a ridge. The vertical displacement has been recorded along these lines and plotted in the Figure 5(a,b). Deformation of different timescales and length-scales has been observed. First, the surface deforms due to the hydrostatic pressure, and then it oscillates around the mean deformation.

For more stiff problems, it would be more efficient to use an implicit/iterative coupling technique. For the current cases, the computational cost of the implicit method is comparable to the explicit techniques. Hence, the implicit approach has not been applied. We anticipate that other solid parameters or higher hydrostatic pressure cases would benefit from an implicit solution technique.

4.3. Turbulent statistics

As a sample quantitative comparison, the average streamwise velocity and turbulent kinetic energy profiles have been compared in Figure 3(b) for all the cases discussed above

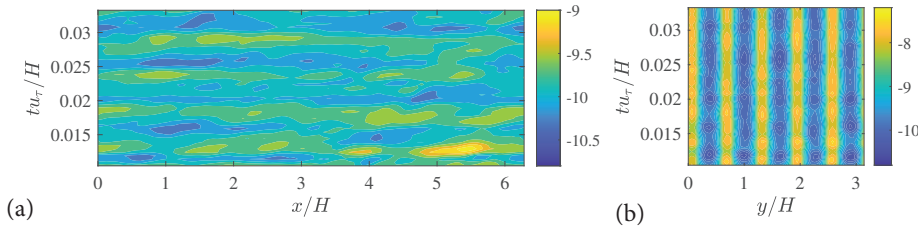


FIGURE 5. Time history of vertical displacement of the top surface at (a) streamwise line-out at $y/H = \pi/2$ and (b) spanwise line-out at $x/H = \pi$.

and compared with the results in Moser *et al.* (1999). Because of surface fluctuations, some grid points inside the boundary layer change the status from fluid to solid. These grid points are excluded from the calculations, and statistics were not collected in that region (several wall units near the interface). The averaging time (tu_τ/H) for the two-way coupled case is approximately 6.4. The hydrostatic deformation has been taken into consideration when normalizing the distance in the wall-normal direction. The condition or the intensity of turbulence in the boundary layer can be quantified by the turbulence kinetic energy profiles, which are plotted in the wall units in Figure 3(b) for the different FSI cases discussed above.

5. Conclusions

A multilevel computational framework is proposed to study the interaction of TBL with an anisotropic compliant layer. The turbulent channel flow over a compliant surface has been explored using a coupled model of the immersed boundary and the nonlinear finite element of the solid domain. The compliant coating resembles structure of dolphin skin with three distinct layers. To identify the most influential parameters, a resolvent analysis is formulated for both hard- and soft-coating layers. One-way coupled simulations are then conducted to explore some of the parameters, followed by two-way coupled FSI simulations for the suitable parameters. The structure shows strong coupling behaviour with flow. Yet, the response of the system is highly sensitive to geometrical and material parameters of the compliant layer, so more elaborate study is needed to identify the most critical conditions. Further simulations with the proposed framework will help us sufficiently represent the energy and momentum flow associated with the interaction of the TBL and viscoelastic coating which will in turn allow careful investigation of the pathways affecting the dominant vortex structures and drag reduction calculation.

REFERENCES

- BABENKO, V. 2021 *Experimental Hydrodynamics for Flow Around Bodies*. Acad. Press.
- BENSCHOP, H., GREIDANUS, A., DELFOS, R., WESTERWEEL, J. & BREUGEM, W.-P. 2019 Deformation of a linear viscoelastic compliant coating in a turbulent flow. *J. Fluid Mech.* **859**, 613–658.
- CARPENTER, P. W., DAVIES, C. & LUCEY, A. D. 2000 Hydrodynamics and compliant walls: Does the dolphin have a secret? *Curr. Sci.* 758–765.
- CHAVARIN, A. & LUHAR, M. 2020 Resolvent analysis for turbulent channel flow with ripples. *AIAA J.* **58**, 589–599.

- DUNCAN, J. H. 1986 The response of an incompressible, viscoelastic coating to pressure fluctuations in a turbulent boundary layer. *J. Fluid Mech.* **171**, 339–363.
- ESTEGHAMATIAN, A., KATZ, J. & ZAKI, T. A. 2022 Spatiotemporal characterization of turbulent channel flow with a hyperelastic compliant wall. *J. Fluid Mech.* **942**, A35.
- FISH, F. E. & ROHR, J. 1999 Review of dolphin hydrodynamics and swimming performance.
- FISHER, D. H. & BLICK, E. F. 1966 Turbulent damping by flabby skins. *J. Aircraft* **3**, 163–164.
- FLORYAN, J. & ZEMACH, C. 1993 Schwarz-christoffel methods for conformal mapping of regions with a periodic boundary. *J. Comput. Appl. Math.* **46**, 77–102.
- FRANCFORT, G. A. & MURAT, F. 1986 Homogenization and optimal bounds in linear elasticity. *Arch. Ration. Mech. Anal.* **94**, 307–334.
- HILBER, H. M., HUGHES, T. J. & TAYLOR, R. L. 1977 Improved numerical dissipation for time integration in structural dynamics. *Earthq. Eng. Struc. Dyn.* **5**, 283–292.
- IVANOV, O., VEDENEV, V., KULIK, V. & BOIKO, A. 2017 The influence of compliant coatings on skin friction in the turbulent boundary layer. *J. Phys.: Conf. Ser.* **894**.
- KAUSEL, E. 1986 Wave propagation in anisotropic layered media. *Int. J. Numer. Meth. Eng.* **23**, 1567–1578.
- KRAMER, M. O. 1962 Boundary layer stabilization by distributed damping. *Nav. Eng. J.* **74** (2), 341–348.
- LUHAR, M. & CHAVARIN, A. 2019 A minimal model for riblet geometry optimization. In *APS Division of Fluid Dynamics Meeting Abstracts*, pp. H26–007.
- LUHAR, M., SHARMA, A. S. & MCKEON, B. 2015 A framework for studying the effect of compliant surfaces on wall turbulence. *J. Fluid Mech.* **768**, 415–441.
- MOSER, R. D., KIM, J. & MANSOUR, N. N. 1999 Direct numerical simulation of turbulent channel flow up to $Re_\tau = 590$. *Phys. Fluids* **11**, 943–945.
- PAIDOUSSIS, M. P. 1998 *Fluid-Structure Interactions: Slender Structures and Axial Flow*, Vol. 1. Acad. Press.
- PATIL, G. U. & MATLACK, K. H. 2021 Review of exploiting nonlinearity in phononic materials to enable nonlinear wave responses. *Acta Mech.* **233**, 1–46.
- RAN, W., ZARE, A. & JOVANOVIĆ, M. R. 2021 Model-based design of riblets for turbulent drag reduction. *J. Fluid Mech.* **906**.
- REESE, S. & GOVINDJEE, S. 1998 A theory of finite viscoelasticity and numerical aspects. *Int. J. Solids Struc.* **35**, 3455–3482.
- ROBINSON, S. K. 1991 Coherent motions in the turbulent boundary layer. *Annu. Rev. Fluid Mech.* **23**, 601–639.
- SEO, J. H. & MITTAL, R. 2011 A high-order immersed boundary method for acoustic wave scattering and low-mach number flow-induced sound in complex geometries. *J. Comput. Phys.* **230**, 1000–1019.
- TONG, P. & MEI, C. 1992 Mechanics of composites of multiple scales. *Comput. Mech.* **9**, 195–210.
- WANG, T.-K. & SHOELE, K. 2021 Geometrically weighted modal decomposition techniques. *J. Fluid Mech.* **911**, A41.
- XU, S., REMPFER, D. & LUMLEY, J. 2003 Turbulence over a compliant surface: numerical simulation and analysis. *J. Fluid Mech.* **478**, 11–34.